Quantifying Time-Averaged Methane Emissions from Individual Coal Mine Vents with GHGSat-D Satellite Observations

Daniel J. Varon[1,2], Daniel J. Jacob[1], Dylan Jervis[2], Jason McKeever[2]

[1]Harvard University, Cambridge, Massachusetts 02138, United States
[2]GHGSat Inc., Montréal, Québec, H2W 1Y5, Canada

Correspondence to: Daniel J. Varon (danielvaron@g.harvard.edu)

Abstract. Satellite observations of atmospheric methane plumes offer a means for global mapping of methane point sources. This capability has so far been demonstrated only for anomalously large or regionally aggregated point sources. Here we use the GHGSat-D satellite instrument with 50-m spatial resolution and 9-19% single-pass column precision to quantify mean source rates for three coal mine vents (San Juan, United States; Appin, Australia; Bulianta, China) under apparently normal operating conditions and over a 2-year period (2016-2018). This involves averaging wind-rotated observations from 13-24 overpasses to achieve satisfactory signal-to-noise. Our wind rotation method optimizes the wind direction information for individual plumes to account for error in meteorological databases. We derive source rates from the time-averaged plumes using integrated mass enhancement (IME) and cross-sectional flux (CSF) methods calibrated with large eddy simulations (LES). We find time-averaged source rates ranging from 2150 to 5690 kg h^{-1} for the three coal mine vents, with about 40% precision, and generally consistent with previous estimates, which are however highly variable. The IME and CSF methods agree within 15%. Our 2300 ± 1020 kg h^{-1} estimate for the San Juan mine is consistent with the annual mean value of 2585 kg h^{-1} for 2017 reported to the United States Greenhouse Gas Reporting Program (GHGRP). Our results demonstrate the potential of space-based monitoring for annual reporting of methane emissions from point sources, and suggest that future satellite instruments with similar pixel resolution but better precision should be able to constrain a wide range of point sources.

INTRODUCTION

Methane is a powerful greenhouse gas with large anthropogenic sources. It has contributed 1.0 W m^{-2} to radiative forcing since pre-industrial times on an emission basis (IPCC, 2013). Underground coal mine vents are among the largest individual point sources of methane (Maasakkers et al., 2016) and are estimated to account for ~10% of global anthropogenic methane emissions (Saunois et al., 2016), but source reporting is highly uncertain. Remote sensing of atmospheric methane by solar backscatter in the shortwave infrared (SWIR) can be effective for quantifying point sources (Jacob et al., 2016; Duren et al., 2019). Krings et al. (2013) used aircraft remote sensing data to quantify methane emissions from coal mine vents in Germany. Frankenberg et al. (2016) conducted an aircraft remote sensing study of coal mine plumes in the Four Corners

region of the Southwest United States and found the emissions to be highly variable and intermittent. Global-observing satellite instruments have demonstrated the capability to characterize methane emissions on regional scales (Turner et al., 2015; Maasakkers et al., 2019; Miller et al., 2019) and from anomalously large sources (Pandey et al., 2019), but are limited by relatively coarse imaging resolution (~10 km). The GHGSat-D satellite instrument overcomes this limitation by conducting high-resolution observations of point sources over targeted domains (Varon et al., 2019). Here we demonstrate the capability of GHGSat-D to observe methane plumes from individual coal mine vents and infer time-averaged source rates.

GHGSat-D was launched in June 2016 as demonstration for a future constellation of small satellites to monitor individual methane point sources from space (Brakeboer, 2015; Sloan et al., 2016). Since then, single-pass GHGSat-D observations have revealed anomalously high-emitting facilities in oil/gas fields with source rates exceeding 10,000 kg h^{-1} (Varon et al., 2019). The largest methane point sources under normal operating conditions are the vents of large underground coal mines, typically in the range 1000-10,000 kg h^{-1} (Krings et al., 2013; Frankenberg et al., 2016; Smith et al., 2017; Jacob et al., 2016). Here we show that time-averaging of wind-rotated GHGSat-D observations can enable detection and quantification of methane emissions from individual coal mine vents, adapting an approach previously applied to satellite observations of point sources for CO (Pommier et al., 2013), SO_2 (Fioletov et al., 2015; McLinden et al., 2016), NO_2 (Valin et al., 2013; de Foy et al., 2015; Zhang et al., 2019), and NH_3 (Clarisse et al., 2019; Dammers et al., 2019), but including significant innovation to account for large errors and limited number of observations. Time-averaging is necessary here to achieve satisfactory signal-to-noise, but it also has the advantage of smoothing over intermittent sources and providing the annual emission estimates most relevant for national emission reporting and global methane budget analyses.

MATERIALS AND METHODS

GHGSat-D observations. GHGSat-D uses a miniature Fabry-Perot interferometer with spectral bandpass 1630-1675 nm (McKeever et al., 2017; Varon et al., 2019). The measurements are made at 50-m effective pixel resolution over ~12×12 km^2 targeted domains. Methane column concentrations are retrieved from the resulting spectra using a 100-layer, clear-sky radiative transfer model in an inverse modelling framework, following Rodgers (2000) and as described by Varon et al. (2019). The inversion retrieves the total column concentrations $\Omega(x,y)$ [mol m^{-2}] of methane across the scene, based on HITRAN absorption line spectra (Gordon et al., 2017) and U.S. Standard Atmosphere vertical profiles (NASA 1976). The column mass enhancement $\Delta\Omega(x,y) = \Omega(x,y) - \Omega_b$ then characterizes the plume relative to the local background column concentration Ω_b [mol m^{-2}] inferred from the scene. The inversion also retrieves albedo, CO_2, and water vapor. The work presented here includes a correction of retrieval errors from aliased surface properties and other measurement parameters (McKeever et al., 2017).

GHGSat-D has an average revisit time of about two weeks, depending on latitude, and requires clear skies for successful observation. Since its launch in June 2016, it has repeatedly targeted the vents of three underground coal mines: the San Juan mine in New Mexico, USA; the Appin mine in New South Wales, Australia; and the Bulianta mine in Inner

Mongolia, China. These coal mines were selected for their large coal production rates and/or previous reports of large methane emissions (SACMS 2011; Frankenberg et al., 2016; Ong et al., 2017; Smith et al. 2017). Here we examine GHGSat-D observations of the coal mine vents taken between August 2016 and December 2018, totalling 13-24 cloud-free observations per mine (see Table 1). The Appin mine was closed beginning on 28 June 2017 due to safety concerns and partially re-opened on 13 October 2017. We discard the four cloud-free observations made during this extended closure, leaving a total of 13 observations for analysis. Several other shorter closures occurred at Appin during the observation period, but these did not overlap with our measurements.

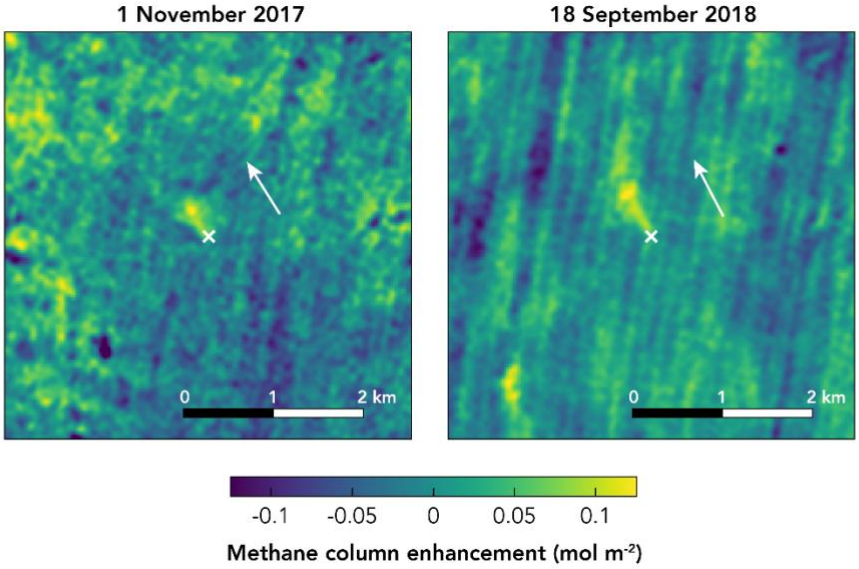

Figure 1: Instantaneous plumes observed by GHGSat-D over the San Juan mine in New Mexico on (a) November 1st, 2017 and (b) September 18th, 2018. The white 'x' symbols mark the location of the coal mine vent (36.792°N, 108.389°W) and the white arrows show wind direction inferred from the orientation of the plumes (see text).

Figure 1 shows methane column enhancements from individual GHGSat-D scenes centred on the San Juan coal mine vent. These scenes were chosen for their detectable plumes, but also illustrate GHGSat-D retrieval artefacts resulting primarily from striping noise, surface reflectance variability, and stray light. Some artefacts are similar in magnitude to the plumes, which highlights the importance of prior knowledge of source location. Column precisions for our San Juan, Appin, and Bulianta observations are estimated at 9%, 19%, and 12% of background, respectively, based on the standard deviations of non-plume column enhancements across the scenes. Most scenes do not feature readily detectable plumes, which motivates our time-averaging analysis.

Wind data for time-averaging. Time-averaging of plume observations to improve signal-to-noise and infer emissions from point sources requires knowledge of wind speed and direction for the individual scenes (Pommier et al., 2013; Valin et al., 2013; de Foy et al., 2015; Fioletov et al., 2015; McLinden et al., 2016; Zhang et al., 2019; Clarisse et al., 2019; Dammers et al., 2019; Hill & Nassar, 2019). Wind information can come from local measurements, from assimilated

meteorological databases, or directly from the plume observations themselves (Jongaramrungruang et al., 2019). The appropriate wind averaging time for an individual scene depends on the lifetime of the detectable plume before turbulent diffusion dilutes it to below detectable levels. It ranges from ~5 minutes for a small plume to ~1 h for a large plume several km in extent (Varon et al., 2018). Coal mine vent plumes as observed by GHGSat-D tend to be small (<1 km in scale; Figure 1) and are therefore best interpreted with an averaging time of about 5 minutes.

Our algorithm to relate plume concentrations to emissions uses 10-m wind information (Varon et al., 2018). We take this information from two hourly meteorological databases: (1) the NASA Goddard Earth Observing System – Fast Processing (GEOS-FP) reanalysis product with full global coverage at 0.25°×0.3125° resolution (Molod et al., 2012), and (2) the DarkSky online weather application programming interface (API) with partial coverage (darksky.net/dev). Comparison with one month of daytime (15:00-21:00 UTC) wind measurements from 10 U.S. airports in the MesoWest database (Horel et al. 2002) suggests that GEOS-FP has more precise wind speed data than DarkSky, while DarkSky has more precise wind direction data. Error standard deviations on hourly average wind speed and direction from GEOS-FP are 1.5 m s^{-1} and 49 degrees relative to the airport measurements, compared to 2.2 m s^{-1} and 37 degrees for DarkSky. We therefore use GEOS-FP winds as default, but substitute DarkSky wind direction where available. DarkSky winds are available for nearly all our observations of the San Juan and Appin mines, but not for Bulianta.

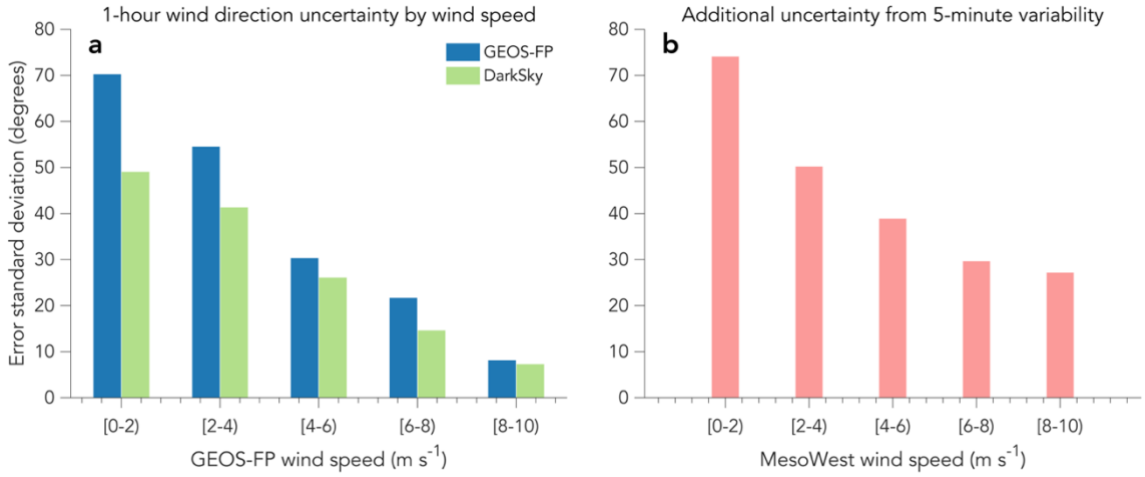

Figure 2: Error in estimating 10-m wind direction from the GEOS-FP and DarkSky datasets. **(a)** Error standard deviations for GEOS-FP and DarkSky hourly average wind direction relative to one month of measurements from 10 U.S. airports (ABQ, ATL, BOS, DFW, LAX, MCI, MSP, PDX, PHL, and PHX) in the MesoWest database, binned by GEOS-FP wind speed. The airport measurements are for daytime June 2017 (15:00–21:00 UTC). **(b)** Additional uncertainty for estimating 5-minute wind direction from 1-hour averages, based on 5-minute wind direction variability in the MesoWest data.

Figure 2 shows the wind direction error statistics when using meteorological reanalysis data to infer local wind direction as referenced by the MesoWest database. The error depends strongly on wind speed, with larger errors at low wind speeds, as would be expected from turbulence. The error on the mean hourly wind in the meteorological databases (Figure 2, left panel) is compounded for small plumes by the error in inferring the more appropriate 5-minute average wind (Figure 2,

right panel), in which case the two errors are added in quadrature. For observations with strong instantaneous plumes (Figure 1), we estimate wind direction directly from the plume axis, which we define from a weighted mean of pixel coordinates with the plume column concentrations as weights. The wind direction error in that case is estimated to be 5 degrees.

For a given point source, a time-averaged plume over the GHGSat-D record can be constructed from the methane column enhancements $\Delta\Omega_i(x,y)$ [mol m^{-2}] observed over the source domain (x,y) on individual days $i = 1 \ldots N$. This is done by (1) georeferencing and aligning the observations on a common grid, (2) rotating each observation around the known source location by the local wind direction θ_i, and (3) computing per-pixel means over the rotated observations. The alignment and rotation steps require precise knowledge of the source location at the scale of the observations. The rotation step may introduce negative bias from wind direction uncertainty, as a mis-rotated plume may be lost in the noisy background of the time-averaged observation. We account for this bias through our source rate retrieval method, as described in the "Estimating source rates" section below.

Optimizing wind directions. Wind direction errors in the meteorological databases are relatively large, particularly for small plumes under low wind conditions (Figure 2). Here we correct the wind directions used for plume rotation in order to maximize concentrations in the time-averaged plume while minimizing deviation from prior wind estimates. Specifically, we maximize the joint Gaussian probability distribution $P(\boldsymbol{\theta})$ given by

$$\log P(\boldsymbol{\theta}) = -\frac{(M(\boldsymbol{\theta})-M_{\max})^2}{\delta^2} - (\boldsymbol{\theta}-\boldsymbol{\theta_a})^T {S_a}^{-1}(\boldsymbol{\theta}-\boldsymbol{\theta_a}) \quad (1)$$

by minimizing $-\log P(\boldsymbol{\theta})$. Here, $\boldsymbol{\theta}$ is a wind direction vector whose elements θ_i, $i = 1 \ldots N$, are the wind directions used to rotate N GHGSat-D observations; $\boldsymbol{\theta_a}$ is a vector of prior wind direction estimates for the observations, from GEOS-FP and DarkSky; S_a is the (diagonal) prior error covariance matrix describing uncertainty in the prior wind direction, which depends on wind speed, plume lifetime (here 5 minutes), and whether the prior is drawn from GEOS-FP, DarkSky, or the plume itself; $M(\boldsymbol{\theta})$ [mol] is the total methane mass (integrated mass enhancement, or IME) in a wedge-shaped mask placed downwind of the source after time-averaging with a set of wind directions $\boldsymbol{\theta}$ (see below); $M_{\max}$ [mol] is the maximum possible value of $M(\boldsymbol{\theta})$ for the set of observations when no constraints are placed on $\boldsymbol{\theta}$; and δ^2 [mol^2] is the error variance in $M(\boldsymbol{\theta})$ due to GHGSat-D measurement noise. We minimize $-\log P(\boldsymbol{\theta})$ numerically using the Nelder-Mead simplex algorithm (Nelder & Mead, 1965; Lagarias et al., 1998).

We rotate individual observations by their wind direction such that the rotated wind is by convention from the north. $M(\boldsymbol{\theta})$ is computed at each iteration of the optimization procedure as the IME over a simple wedge-shaped mask extending 500 m south and ±15 degrees of south. The IME is the sum of column enhancements $\Delta\Omega(x,y)$ over the mask, multiplied by the pixel area. We then compute $M_{\max}$ by rotating the mask around the source location by 360 degrees in each observation, recording for each the maximum IME, and averaging over all observations. To calculate δ, we perform time averaging using our prior wind directions, and then compute the IME within the wedge-shaped mask when placed at 100 random non-plume locations across the time-averaged domain; the standard deviation of these results gives δ.

Defining plume boundaries. Inferring source rates from plume observations requires a mask that distinguishes plume pixels from the image background. Varon et al. (2018) suggested a *t*-test procedure for isolating plumes from normally distributed measurement noise, but that procedure's performance is limited here by systematic errors in the time-averaged observations. Instead, we isolate the plumes by applying an enhancement threshold at the 98th percentile of $\Delta\Omega(x, y)$ over the time-averaged domain. This defines a threshold mask for the scene. To delete random classification errors and reduce loss of plume enhancements at mask edges due to thresholding, we smooth the masks with a 150×150 m2 median filter, which replaces each pixel's value with the median of its 150×150 m2 neighbourhood, followed by a Gaussian filter with standard deviation 50 m. Wind rotation and time averaging smooth out most of the observation artefacts such as those seen in Figure 1, but some still remain in the mask. For the purpose of inferring point source rates, we only consider the continuous portion of the mask originating from the source location.

Estimating source rates. We estimate source rates for our time-averaged plumes using two different methods: the IME method and the cross-sectional flux (CSF) method (Varon et al., 2018). The IME method relates the source rate Q [mol s-1] to the detectable plume mass IME [mol] in terms of an effective wind speed $U_{\text{eff,IME}}$ [m s-1] and plume size L [m]:

$$Q = \frac{U_{\text{eff,IME}}}{L}\,\text{IME} = \frac{U_{\text{eff,IME}}}{L}\sum_{j=1}^{n}\overline{\Delta\Omega}(x_j, y_j)A_j, \quad (2)$$

where $\overline{\Delta\Omega}(x_j, y_j)$, $j = 1 \ldots n$, is the time-averaged column concentration of the jth plume pixel with coordinates (x_j, y_j) and area A_j, and the summation is over the n pixels within the continuous plume mask originating from the source location. The plume size L is defined following Varon et al. (2018) as the square root of the plume mask's area. The effective wind speed $U_{\text{eff,IME}}$ is an operational parameter that is inferred from the local 10-m wind speed U_{10} in a manner that depends on the definitions of the plume mask and size. We discuss the $U_{\text{eff}} = f(U_{10})$ relationship below.

The CSF method originally introduced by White (1976) and adapted to column observations by Krings et al. (2011, 2013) and Varon et al. (2018) relates Q to a cross-plume concentration integral [mol m-1] and a different effective wind speed $U_{\text{eff,CSF}}$ than in the IME method:

$$Q = U_{\text{eff,CSF}}\int_a^b \overline{\Delta\Omega}(x, y)dy. \quad (3)$$

Here the x-axis is defined by the wind direction (northerly by convention for our time-averaged plumes) and the y-axis is perpendicular to the wind direction. The integral is computed between the plume boundaries $[a, b]$ defined by the plume mask, and this computation can be done at multiple downwind distances x to improve estimation of Q through averaging. Here we repeat the calculation at pixel-width intervals across the full extent of the detectable plume.

The effective wind speeds in the IME and CSF methods are operational parameters that can be related to the local 10-m wind speed U_{10}. Varon et al. (2018) calibrated $U_{\text{eff}} = f(U_{10})$ relationships for instantaneous plumes generated by large eddy simulation (LES), but the relationships may be different here for two reasons. First, we use a different definition of the plume mask, as described in the previous section. This affects the dependence of IME and plume transects on Q. Second, the

dependences of IME (or plume transects) on wind speed and source rate may be different for time-averaged compared to instantaneous plumes.

Here we calibrate new $U_{\text{eff}} = f(U_{10})$ relationships for the IME and CSF methods, customized to our observing conditions and plume mask. To do this, we repeat the LES plume analysis of Varon et al. (2018) on the same ensemble of simulations, but with time-averaged rather than instantaneous plumes. The LES ensemble comprises 15 five-hour simulations with a range of wind speeds and boundary layer depths. We calibrate $U_{\text{eff}} = f(U_{10})$ relationships for each coal mine independently, since for each we have a different number of observations and level of background noise. We use the following procedure. First, a number of LES plume snapshots are randomly drawn from the ensemble (24 for San Juan, 13 for Appin, and 14 for Bulianta). The source rate for the plumes is set to 2500 kg h^{-1} as a typical value for large coal mine vent emissions (Jacob et al., 2016); this only affects the size of the detectable plumes and hence the plume mask. Each snapshot is rotated by a random wind direction, and the 5-minute average value of U_{10} at the source location is recorded. We corrupt the plume snapshots with normally distributed, spatially uncorrelated noise of mean zero and standard deviation dependent on the observation conditions of each mine (9%, 19%, or 12% of a 1850 ppb background). We then follow the wind direction optimization procedure outlined above (Eq. 1) to recover the LES plume wind directions from the randomly corrupted prior estimates, and assemble in this manner a time-averaged plume pseudo-observation. After constructing the plume mask and calculating IME, L, and the mean transect for the time-averaged plume, we use equations (2) and (3) to compute U_{eff} based on prior knowledge of Q (2500 kg h^{-1}). Meanwhile, we compute U_{10} for the time-averaged observation as the mean of the 5-minute averages across aggregated plumes. We repeat this procedure 100 times on a set of LES plumes comprising 80% of the ensemble (~2900 plume snapshots), simulating 100 time-averaged plumes. We then derive the $U_{\text{eff}} = f(U_{10})$ relationships by least squares fitting. Finally, to quantify source rate retrieval error, we evaluate these relationships on time-averaged plumes constructed from the remaining 20% of the LES plume ensemble (see Supplemental Information).

Figure 3 shows our derived $U_{\text{eff}} = f(U_{10})$ relationships for the three coal mines. We find that linear relationships without intercepts capture the behaviour well in all cases, but the slopes depend on the number of observations aggregated, level of measurement noise, and wind direction prior error variance. As detecting the source becomes more difficult (due to fewer observations being available, stronger measurement noise, and/or worse wind direction priors), the slopes steepen to make up for loss of mass at the plume boundaries. The winds are fit by robust linear regression, which assigns less weight to outlier points, to mitigate the considerable scatter in U_{eff} for larger values of U_{10}. $U_{\text{eff}} = f(U_{10})$ slopes for the CSF method are similar to the results of Varon et al. (2018), but slopes for the IME method are significantly different.

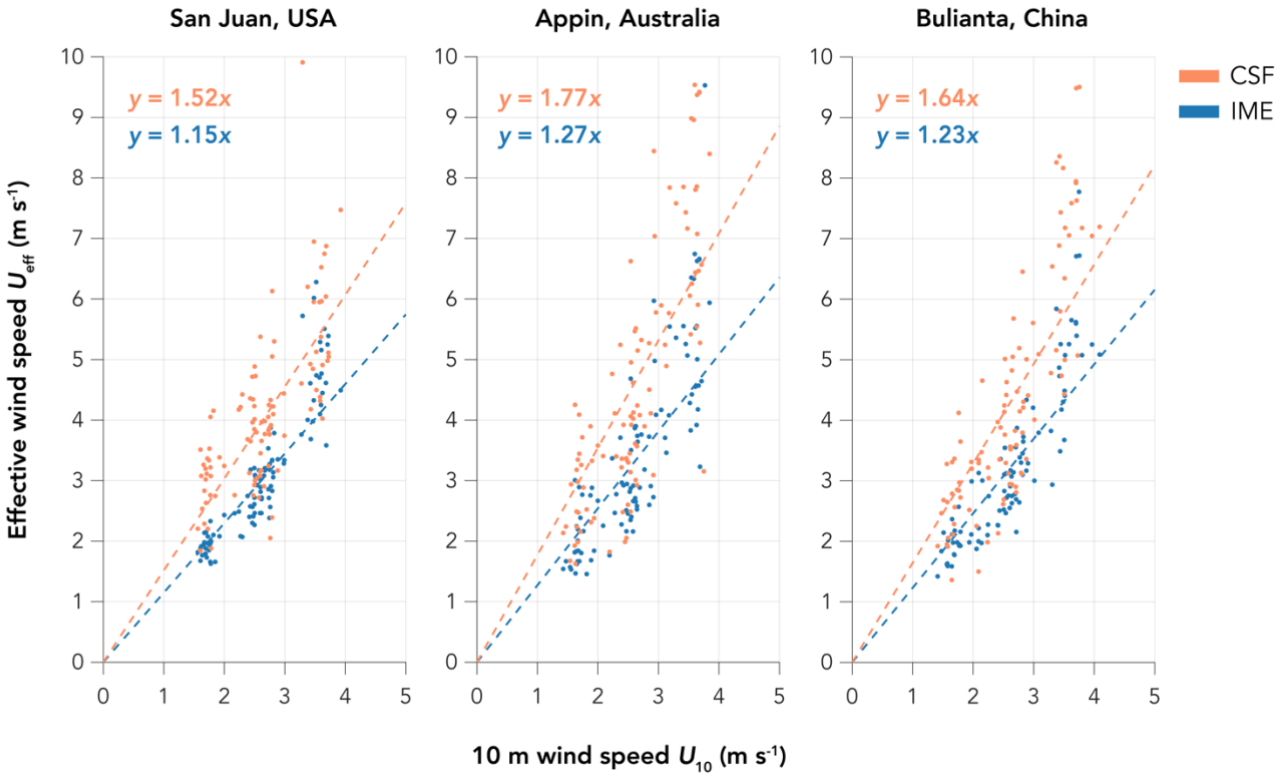

Figure 3: Effective wind speeds U_{eff} for retrieving time-averaged methane source rates by the integrated mass enhancement (IME) and cross-sectional flux (CSF) methods (Eq. 3 and 4) as a function of the time-averaged 10-m wind speed U_{10}. The $U_{\text{eff}} = f(U_{10})$ relationships are derived from large eddy simulations (LES) of instantaneous methane plumes, with time-averaging and wind rotation corresponding to our measurement conditions for (a) San Juan, (b) Appin, and (c) Bulianta. Each point represents a time-averaged plume assembled from LES instantaneous plumes, with the level of background noise and number of observations adapted to the mine of interest (see Table 1). The functions are fit by robust least squares (see text).

RESULTS AND DISCUSSION

Time-averaged plumes. Figure 4 shows our time-averaged rotated observations of the San Juan, Appin, and Bulianta coal mine vents, both before and after wind direction optimization. The plumes are oriented to the south of the source location by convention, and are separated from the noisy background by thresholding and smoothing as discussed in the "Defining plume boundaries" section. Enhancements above the threshold but not directly downwind of the source location are ignored as retrieval artefacts.

Before optimizing wind direction to improve plume-to-noise contrast, the San Juan and Appin mine vents show strong time-averaged plumes with respective peak enhancements 7% and 20% above background. The Bulianta mine vent shows peak downwind enhancements 8% above background, but a less distinctive plume shape. One possible explanation for this is that the Bulianta vent is at the base of a hill, leading to large and potentially systematic wind direction error, in contrast to the San Juan and Appin vents, which are in flat terrain. Optimizing wind direction amplifies the plumes' mean

enhancements by 11-13% and produces a more elongated plume shape for the Bulianta coal mine, with peak methane enhancements more than 10% above background. Peak plume enhancements do not generally appear at the source location, contrary to what one would expect. This could be because of systematic retrieval errors over the vent location (for example due to surface reflectance variability or aerosol particles in the plume). Missing large enhancements near the vent could lead to a low bias in IME emission rate estimates, but would have a smaller effect on the CSF method, where each cross-plume integral downwind of the source independently approximates the emissions.

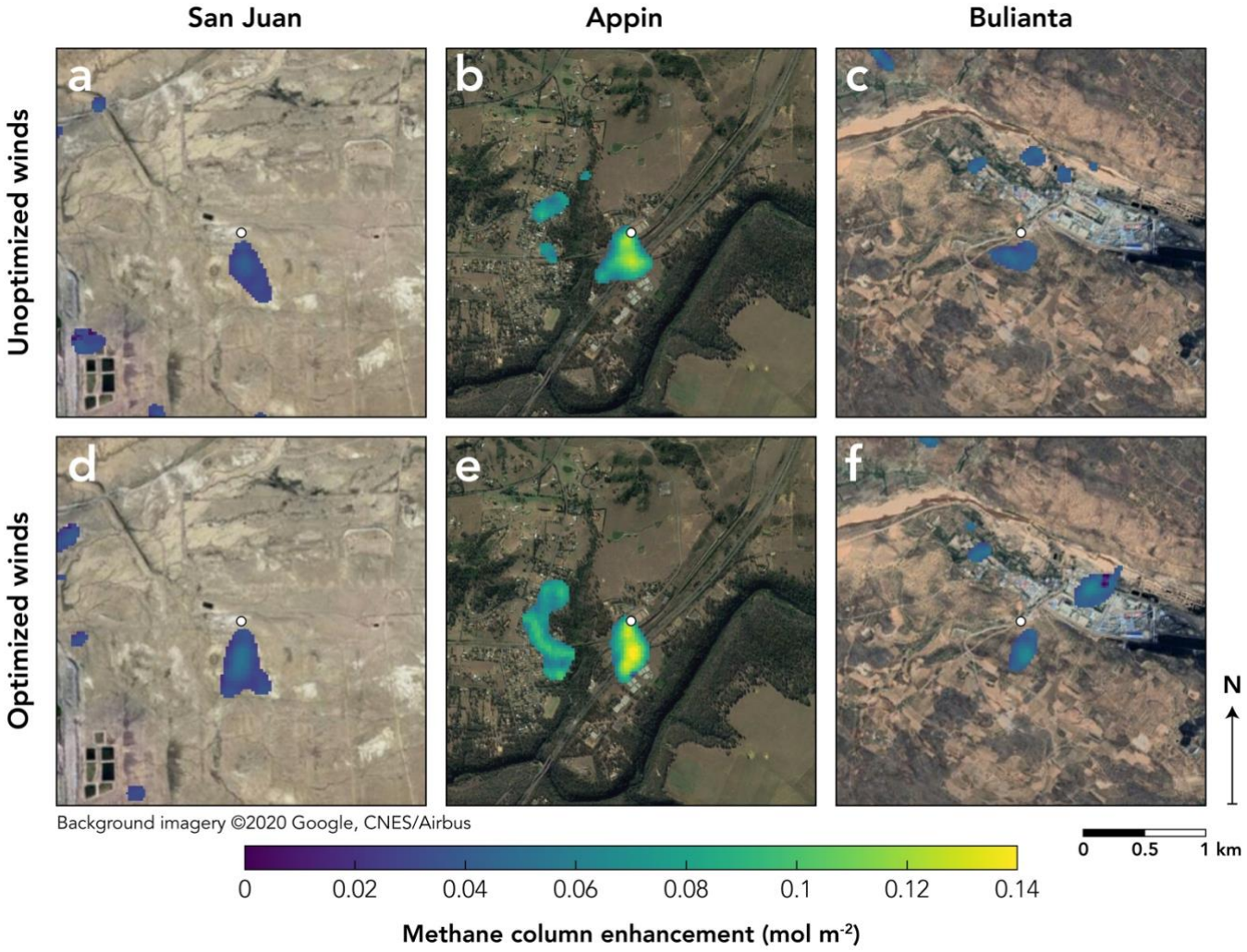

Figure 4: Time-averaged methane plumes from the San Juan, Appin, and Bulianta coal mine vents, as observed by GHGSat-D from August 2016 through December 2018. The single-pass observations have been rotated to a northerly wind direction using (a-c) local wind data from GEOS-FP and DarkSky and (d-f) optimized wind directions with GEOS-FP and DarkSky winds as prior estimates (see text). The methane column enhancements are overlaid on Google Earth Pro imagery after thresholding and smoothing with median and Gaussian filters (see text). The white markers show the locations of the coal mine vents in the centre of each scene.

Time-averaged source rates. Table 1 shows our time-averaged source rate estimates for the San Juan, Appin, and Bulianta mines determined from the wind-optimized plumes. Estimates from the IME and CSF methods agree within their

error standard deviations, which is a first check that our effective wind speed functions are well-calibrated. We estimate mean emissions of 2300 ± 1020 kg h^{-1} for the San Juan vent, 5690 ± 2540 kg h^{-1} for the Appin vent, and 2600 ± 1010 kg h^{-1} for the Bulianta vent using the IME method. The estimates are 7-13% lower using the CSF method, contradicting the possibility of low bias in the IME method. The uncertainties are about 40% and incorporate wind speed error, error in the IME and CSF models (including wind direction error and uncertainty in the effective wind speed fits of Fig. 3), and correlated random noise in the retrieved columns. A detailed error analysis is presented in the Supplemental Information.

Also shown in Table 1 are previous emission estimates for each of the mine vents, all from much smaller samples and/or durations. Frankenberg et al. (2016) estimated emissions of 360-2800 kg h^{-1} for the San Juan vent based on several days of aircraft remote sensing measurements, and Smith et al. (2017) inferred mean emissions of 1446 kg h^{-1} from five days of aircraft mass balance measurements during the same period. Quarterly in-situ measurements of the vent flow rate and methane concentration reported to the United States Environmental Protection Agency (EPA) in 2017 put emissions from the San Juan vent at 2585 kg h^{-1} averaged over the year (EPA, 2017), in remarkable agreement with our estimate. Ong et al. (2017) approximated emissions of 10,800-12,600 kg h^{-1} from the Appin mine, based on estimates of the vent flow rate and air stream methane concentration. Cardno (2009) used coal production activity data and Australian National Greenhouse Accounts (NGA) emission factors to estimate ventilation shaft methane emissions of ~5200 kg h^{-1} for the Appin mine in a two longwall mining formation. We are aware of only one emission estimate for the Bulianta mine: 170 kg h^{-1}, reported by the Chinese State Administration for Coal Mine Safety (SACMS). This estimate is based on ground measurements made during a 2-3 month safety evaluation performed in 2011 and is much lower than our result. Emissions from coal mine vents have large temporal variability, as shown by the Frankenberg et al. (2016) observations for San Juan, and satellite observations have unique value in providing long-term averages.

In summary, our results demonstrate the capability of space-based observations of methane plumes to quantify point source rates from high-emitting facilities under apparently normal operating conditions. The GHGSat-D demonstration satellite instrument used in our work has fine spatial resolution (50-m) but coarse single-pass column retrieval precision (9-19%) and large retrieval artefacts. Nevertheless, we were able to quantify time-averaged methane emissions from large coal mine vents (>1000 kg h^{-1}) with ~40% uncertainty. This involved averaging 13-24 observations per target over a 2-year period, using an optimized wind rotation procedure. Our time-averaged result for the San Juan coal mine vent was in close agreement with the annual emission reported to the U.S. EPA. Future methane-observing satellite instruments with similar spatial resolution but improved precision, including GHGSat-C1 to be launched in 2020 (Jervis et al., 2019) and the next generation of orbiting hyperspectral surface imagers (Cusworth et al., 2019), will likely improve our ability to detect methane plumes from individual facilities and infer source rates. Quantifying sources down to 100 kg h^{-1} would account for more than 90% of emissions from point sources in the U.S. GHGRP (Jacob et al., 2016). Such thresholds for detection and quantification will continue to shrink as revisit rates for time-averaging increase with the number of instruments in orbit. In view of the large temporal variability of emissions from individual facilities, repeated measurements from satellites may be particularly useful for estimating annual emissions for facility-level reporting purposes.

Table 1: Methane source rates from coal mine vents retrieved with GHGSat-D

Coal mine	San Juan	Appin	Bulianta
Location			
Country	United States	Australia	China
State/Region	New Mexico	New South Wales	Inner Mongolia
Latitude	36.7928°N	34.1815°S	39.3835°N
Longitude	108.3890°W	150.7197°E	110.0951°E
Source retrieval metadata			
Averaging period	Aug 2016 – Nov 2018	Nov 2016 – Oct 2018	Aug 2016 – Dec 2018
Number of clear-sky observations	24	13	14
Single-pass error level	9%	19%	12%
10-m wind speed (m s^{-1}) [a]	3.0 (0.5, 8.0)	2.2 (0.7, 3.8)	3.6 (0.9, 9)
Source rate estimates (kg h^{-1}) [b]			
IME method	2300 ± 1020	5690 ± 2540	2600 ± 1010
CSF method	2150 ± 980	5030 ± 2100	2410 ± 970
Previous estimates	360-2800[c], 2585[d], 1446[e]	5200[f], 10800-12600[g]	170[h]

[a] Mean (minimum, maximum) hourly wind speed for the ensemble of observations, obtained from the GEOS-FP database.
[b] The reported source rates are for time-averaged plumes after wind direction optimization (Figure 4), and using either the integrated mass enhancement (IME) or cross-sectional flux (CSF) method.
[c] Range from several days of aircraft remote sensing measurements in April 2015 (Frankenberg et al., 2016).
[d] Annual mean estimate for 2017 from quarterly in-situ measurements of flow rate and methane concentration (EPA, 2017).
[e] Mean estimate from five days of in-situ aircraft mass balance measurements (Smith et al., 2017).
[f] Estimate based on annual coal production activity data and emission factors (Cardno, 2009; converted from kt CO_2e a^{-1}).
[g] Estimate based on ventilation flow rate and air stream methane concentration from vent design (Ong et al., 2017).
[h] Estimate from in-situ measurements during a weeks-long safety evaluation in 2011 (SACMS, 2011).

Competing interests

The authors declare no competing interests.

Acknowledgements

We thank O. B. A. Durak and J. J. Sloan for their roles in developing the GHGSat retrievals algorithm and measurement concept. We thank C. Herzog, M. Arias, K. Wisniewski, M. Latulippe, N. Brown, and J. Thompson for technical assistance and preparation of the GHGSat-D methane data. We also thank J. D. Maasakkers for helpful discussion. D. J. J. was supported by the Carbon Monitoring System of the NASA Earth Science Division.

TOC/Abstract Graphic (for Table of Contents Only)

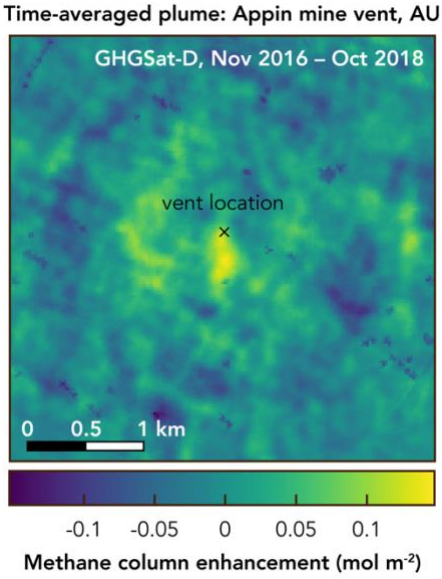

References

Brakeboer, B. N. A. (2015): Development of the structural and thermal control subsystems for an Earth observation microsatellite and its payload. MSc Thesis, University of Toronto, 2015.

Cardno (2009). Environmental Assessment Appin Colliery Area 7 Goaf Gas Drainage Project. Available at https://www.south32.net/docs/default-source/illawarra-coal/bulli-seam-operations/appin/appin-surface-gas-management-project---enviro-asse/environmental-assessment-appin-surface-gas-management-project.pdf?sfvrsn=321a9200_4 (last access: 14 February 2020).

China State Administration of Coal Mine Safety (SACMS, 2011). *Compilation of National Coal Mine Gas Level Identification for 2011* (National Coal Mine Safety Supervision Bureau, 2019).

Clarisse, L., Van Damme, M., Clerbaux, C., and Coheur, P.-F. (2019). Tracking down global NH_3 point sources with wind-adjusted superresolution. *Atmos. Meas. Tech. Discuss.* https://doi.org/10.5194/amt-2019-99

Clerbaux, C., Boynard, A., Clarisse, L., George, M., Hadji-Lazaro, J., Herbin, H., et al. (2009). Monitoring of atmospheric composition using the thermal infrared IASI/MetOp sounder, *Atmos. Chem. Phys.*, 9, 6041–6054, https://doi.org/10.5194/acp-9-6041-2009

Cusworth, D. H., Jacob, D. J., Varon, D. J., Chan Miller, C., Liu, X., Chance, K., et al. (2019): Potential of next-generation imaging spectrometers to detect and quantify methane point sources from space. *Atmos. Meas. Tech.* https://doi.org/10.5194/amt-2019-202

Dammers, E., McLinden, C. A., Griffin, D., Shephard, M. W., Van Der Graaf, S., Lutsch, E., et al. (2019). NH_3 emissions from large point sources derived from CrIS and IASI satellite observations. *Atmos. Chem. Phys.*, 19, 12261–12293. https://doi.org/10.5194/acp-19-12261-2019

DarkSky: DarkSky weather application programming interface (API), available at: https://darksky.net/dev (last access: 9 May 2019), 2019.

De Foy, B., Lu., Zifeng, Streets, D. G., Lamsal, L. N., Duncan, B. N. (2015). Estimates of power plant NO_x emissions and lifetimes from OMI NO_2 satellite retrievals. *Atmospheric Environment*, 116, 1–11. https://doi.org/10.1016/j.atmosenv.2015.05.056

Drummond, J. R. (1992). Measurements of Pollution in the Troposphere (MOPITT). In *The Use of EOS for Studies of Atmospheric Physics*, edited by J. C. Gille and G. Visconti, pp. 77–101, North-Holland, New York.

Duren, R.M., Thorpe, A.K., Foster, K.T., Rafiq, T., Hopkins, F. M., Yadav, V., et al. (2019). California's methane super-emitters. Nature 575, 180–184. doi:10.1038/s41586-019-1720-3

Fioletov, V. E., McLinden, C. A., Krotkov, N., & Li, C. (2015). Lifetimes and emissions of SO_2 from point sources estimated from OMI. *Geophys. Res. Lett.* 42(6), 1969–1976. https://doi.org/10.1002/2015GL063148

Frankenberg, C., Thorpe, A. K., Thompson, D. R., Hulley, G., Kort, E. A., Vance, N., et al. (2016). Airborne methane remote measurements reveal heavy-tail flux distribution in Four Corners region. *Proc. Natl. Acad. Sci. USA* 113, 9734–9739. https://doi.org/10.1073/pnas.1605617113

Global Modeling and Assimilation Office (GMAO): GEOS-FP, available at: https://portal.nccs.nasa.gov/cgi-lats4d/opendap.cgi?&path=, last access: 19 December 2018.

Gordon, I. E., Rothman, L.S., Hill, C., Kochanov, R. V., Tan, Y., Bernath, P. F., et al. (2017). The HITRAN2016 Molecular Spectroscopic Database. *J. Quant. Spectrosc. Radiat. Transfer* 203, 3–69. https://doi.org/10.1016/j.jqsrt.2017.06.038

Hill, T. and Nassar, R. (2019). Pixel size and revisit rate requirements for monitoring power plant CO_2 emissions from space. *Remote Sens.* 11(13), 1608. https://doi.org/10.3390/rs11131608

Horel, J., Splitt, M., Dunn, L., Pechmann, J., White, B., Ciliberti, C., et al. (2002). MesoWest: Cooperative Mesonets in the Western United States. American Meteorological Society February 2002, 211–225. https://doi.org/10.1175/15200477(2002)083<0211:MCMITW>2.3.CO;2

International Panel on Climate Change (IPCC)(2013). *Climate change 2013: The physical science basis. Contribution of Working Group I to the Fifth Assessment Report of the Intergovernmental Panel on Climate Change* (IPCC, Cambridge University Press, New York, 2013).

Jacob, D. J., Turner, A. J., Maasakkers, J. D., Sheng, J., Sun, K., Liu, X., et al. (2016). Satellite observations of atmospheric methane and their value for quantifying methane emissions. *Atmos. Chem. Phys.* 16, 14371–14396. https://doi.org/10.5194/acp-16-14371-2016

Jervis, D., McKeever, J., Gains, D., Varon, D. J., Germain, S., Sloan, J. J., et al. (2018). High-Resolution CH_4 Enhancement Observations near Industrial Sites using the GHGSat-D Demonstration Satellite. Abstract presented at the American Geophysical Union 2018 Fall Meeting, Washington, DC, 10–14 December 2018.

Jervis, D., McKeever, J., Strupler, M., Gains, D., Tarrant, E., & Germain, S. (2019). Rapid Design, Build and Characterization Cycle of the GHGSat Constellation. Abstract presented at the American Geophysical Union 2019 Fall Meeting, San Francisco, CA, 9-13 December 2019.

Jongaramrungruang, S., Frankenberg, C., Matheou, G., Thorpe, A., Thompson, D. R., Kuai, L., & Duren, R.: Towards accurate methane point-source quantification from high-resolution 2D plume imagery. *Atmos. Meas. Tech. Discuss.* https://doi.org/10.5194/amt-2019-173

Krings, T., Gerilowski, K., Buchwitz, M., Reuter, M., Tretner, A., Erzinger, J., et al. (2011). MAMAP – a new spectrometer system for column-averaged methane and carbon dioxide observations from aircraft: retrieval algorithm and first inversions for point source emission rates, *Atmos. Meas. Tech.*, 4, 1735–1758. https://doi.org/10.5194/amt-4-1735-2011

Krings, T., Gerilowski, K., Buchwitz, M., Hartmann, J., Sachs, T., Erzinger, J., et al. (2013). Quantification of methane emission rates from coal mine ventilation shafts using airborne remote sensing data, *Atmos. Meas. Tech.*, 6, 151–166. https://doi.org/10.5194/amt-6-151-2013

Lagarias, J. C., Reeds, J. A., Wright, M. H., & Wright, P. E. (1998). Convergence Properties of the Nelder-Mead Simplex Method in Low Dimensions. *SIAM J. Optim.* 9(1), 112–147. https://doi.org/10.1137/S1052623496303470

Levelt, P. F., Van den Oord, G. H. J., Dobber, M. R., Malkki, A., Visser, H., de Vries, J., Stammes, P., et al. (2006). The Ozone Monitoring Instrument. *IEEE Trans. Geosci. Remote Sensing*, 44, 1093–1101, https://doi.org/10.1109/TGRS.2006.872333

Maasakkers, J. D., Jacob, D. J., Sulprizio, M. P., Turner, A. J., Weitz, M., Wirth, T., et al. (2016). Gridded National Inventory of U.S. Methane Emissions. *Environ. Sci. Technol.*, 50, 23, 13123–13133. https://doi.org/10.1021/acs.est.6b02878

Maasakkers, J. D., Jacob, D. J., Sulprizio, M. P., Scarpelli, T. R., Hannah, N., Sheng, J., et al. (2019). Global distribution of methane emissions, emission trends, and OH concentrations and trends inferred from an inversion of GOSAT satellite data for 2010–2015. *Atmos. Chem. Phys.*, 19, 7859–7881, https://doi.org/10.5194/acp-19-7859-2019

McKeever, J., Durak, B. O. A., Gains, D., Varon, D. J., Germain, S., & Sloan, J. J. (2017). GHGSat-D: Greenhouse gas plume imaging and quantification from space using a Fabry-Perot imaging spectrometer. Abstract presented at the American Geophysical Union 2017 Fall Meeting, New Orleans, LA, 11–15 December 2017.

McLinden, C. A., Fioletov, V., Shephard, M. W., Krotkov, N., Li, C., Martin, R. V., et al. (2016). Space-based detection of missing sulfur dioxide sources of global air pollution. *Nat. Geo.*, 9, 496–500. https://doi.org/10.1038/NGEO2724

Miller, S. M., Michalak, A. M., Detmers, R. G., Hasekamp, O. P., Bruhwiler, L. M. P., & Schwietzke, S. (2019). China's coal mine methane regulations have not curbed growing Emissions. *Nat. Comm.*, 10, 303. https://doi.org/10.1038/s41467-018-07891-7

Molod, A., Takacs, L., Suarez, M., Bacmeister, J., In-Sun, S., & Eichmann, A. (2012). *The GEOS-5 Atmospheric General Circulation Model: Mean Climate and Development from MERRA to Fortuna* (Technical Report Series on Global Modeling and Data Assimilation, Volume 28, NASA, 2012).

Nelder, J. A. and Mead, R. (1965). A Simplex Method for Function Minimization. *The Computer Journal*, 7(4), 308–313. https://doi.org/10.1093/comjnl/7.4.308

Ong, C., Day, S., Halliburton, B., Marvig, P., & White, S. (2017). *Regional Methane Emissions in NSW CSG Basins* (Final Report, CSIRO, Australia, 2017).

Pandey, S., Gautam, R., Houweling, S., Denier van der Gon, H., Sadavarte, P., Borsdorff, T., et al. (2019). Satellite observations reveal extreme methane leakage from a natural gas well blowout. *Proceedings of the National Academy of Sciences*. https://doi.org/10.1073/pnas.1908712116

Pommier, M., McLinden, C. A., & Deeter, M. (2013). Relative changes in CO emissions over megacities based on observations from space. *Geophys. Res. Lett.* 40(14), 3766–3771. https://doi.org/10.1002/grl.50704

Rodgers, C. D. (2000). Inverse methods for atmospheric sounding: theory and practice (Vol. 2). World Scientific.

Saunois, M., Bousquet, P., Poulter, B., Peregon, A., Ciais, P., Canadell, J. G., et al. (2016). The Global Methane Budget 2000-2012. *Earth Syst. Sci. Data*, 8, 697–751. https://doi.org/10.5194/essd-8-697-2016

Sloan, J. J., Durak, B., Gains, D., Ricci, F., McKeever, J., Lamorie, J., et al. (2016). Fabry-Perot interferometer based satellite detection of atmospheric trace gases. *US 9,228,897 B2*, United States Patent and Trademark Office. Retrieved from https://patentimages.storage.googleapis.com/85/4e/65/b3f964823f2f3b/US9228897.pdf

Smith, M. L., Gvakharia, A., Kort, E. A., Sweeney, C., Conley, S. A., Faloona, I., et al. (2017). Airborne Quantification of Methane Emissions over the Four Corners Region. *Environmental Science and Technology* 51(10), 5832–5837. https://doi.org/10.1021/acs.est.6b06107

Thompson, D. R., Thorpe, A. K., Frankenberg, C., Green, R. O., Duren, R., Guanter, L., et al. (2016). Space-based remote imaging spectroscopy of the Aliso Canyon CH_4 superemitter. *Geophys. Res. Lett.*, 43(12), 6571–6578. https://doi.org/10.1002/2016GL069079

United States National Aeronautics and Space Agency (NASA, 1976). *U.S. Standard Atmosphere, 1976* (Technical Report NASA-TM-X-74335, NASA, 1976). https://ntrs.nasa.gov/search.jsp?R=19770009539

United States Environmental Protection Agency (EPA): Facility Level Information on Greenhouse Gases Tool (FLIGHT), available at: https://ghgdata.epa.gov/ghgp/service/html/2017?id=1009342&et=undefined via https://ghgdata.epa.gov/ghgp/main.do (last access: 1 July 2019), 2017.

University of Utah: MesoWest database, available at: http://mesowest.utah.edu/ (last access: 21 November 2017), 2018.

Valin, L. C., Russell, A. R. and Cohen, R. C. (2013). Variations of OH radical in an urban plume inferred from NO_2 column measurements, *Geophys. Res. Lett.*, 40(9), 1856–1860. https://doi.org/10.1002/grl.50267

Varon, D. J., Jacob, D. J., McKeever, J., Jervis, D., Durak, B. O. A., Xia, Y., & Huang, Y. (2018). Quantifying methane point sources from fine-scale satellite observations of atmospheric methane plumes. *Atmos. Meas. Tech.* 11, 5673–5686. https://doi.org/10.5194/amt-11-5673-2018

Varon, D. J., McKeever, J., Jervis, D., Maasakkers, J. D., Pandey, S., Houweling, S., Aben, I., Scarpelli, T., Jacob, D. J. (2019). Satellite discovery of anomalously large methane emissions from oil/gas production. *Geophys. Res. Lett.* 46(22) 13507–13516. https://doi.org/10.1029/2019GL083798

Zavala-Araiza, D., (2019). MethaneSAT: mapping global oil and gas methane emissions to accelerate mitigation. Abstract presented at the 2019 Industrial Methane Measurements conference, Rotterdam, NL, 22–23 May 2019.

Zhang, Y., Gautam, R., Zavala-Araiza, D., Jacob, D. J., Zhang, R., Zhu, L., et al. (2019). Satellite-observed changes in Mexico's offshore gas flaring activity linked to oil/gas regulations. *Geophys. Res. Lett.* 46, 1879–1888. https://doi.org/10.1029/2018GL081145